AIAA JOURNAL
Vol. 38, No. 6, June 2000

Experimental Investigation of the Confluent Boundary Layer of a High-Lift System

F. O. Thomas,* R. C. Nelson,* and X. Liu†
University of Notre Dame, Notre Dame, Indiana 46556

A fundamental experimental investigation is described of the structure and streamwise development of a confluent boundary layer generated by the interaction of a leading-edge slat wake with the turbulent boundary layer on the main element of a multi-element airfoil model. The slat and airfoil model geometry are both fully two dimensional. The research is performed in an attempt to investigate the flow physics of confluent boundary layers and to build an archival database on the interaction of the slat wake and the main element wall layer. In addition, an attempt is made to identify clearly the role that slat wake/airfoil boundary-layer confluence has on lift production and how this occurs. Although complete laser Doppler velocimetry flow surveys were performed for a variety of slat gap and overhang settings, the focus is on two cases representing both strong and weak wake boundary-layer confluence. For those interested in performing numerical simulations, the full database is available from the authors.

I. Introduction

THE lift augmentation that occurs in multi-element airfoils may be described in terms of simple inviscid mechanisms as described by Smith.[1] For example, the influence of a leading-edge slat on high-lift system performance can be explained by considering the loaded slat as a bound vortex that creates a downwash flowfield over the main element leading edge and reduces the magnitude of the suction pressure peak. The lowering of the pressure peak over the main element reduces the severity of the adverse pressure gradient and thereby lessens the chance of flow separation. This allows the main element airfoil to be placed at a higher angle of attack than would be possible without the slat, thus improving the lift capability of the system. In a similar manner, the bound vorticity associated with the loaded trailing-edge flap gives rise to an upwash at the trailing edge of the main element. This upwash acting in conjunction with the Kutta condition effectively increases the loading over the main wing. This is equivalent to an increase in the suction pressure distribution and, consequently, the lift force generated by the main element.

Although simple inviscid arguments like those just outlined can be used to qualitatively describe how a multi-element airfoil generates high lift, it is well known that the actual performance is dominated by numerous viscous effects that loom quite large when one attempts an optimal high-lift system design. As an example, consider the interaction of the wake generated by the leading-edge slat with the boundary layer over the main airfoil element. The orientation of the slat and its geometric spacing relative to the main wing element is one obvious controlling factor on the extent of the slat wake/main element boundary-layer interaction. As the gap between the slat and wing is made smaller, the slat wake will begin to merge with the wing boundary layer. This mixing of a wake from an upstream body with the boundary layer on a downstream element is commonly referred to as a confluent boundary layer. The location of onset of confluence moves forward on the wing as the slat gap is decreased. The resulting confluent viscous layer will be thicker than the main element boundary layer alone, which increases the likelihood of flow separation on the main element at large attack angles.

The computation of flow over multi-element wings requires the ability to successfully model certain high-lift system building block flows, which we define as generic components of the flowfield over any modern high-lift system. These include (in no particular order) 1) leading-edge transition mechanism; 2) a variety of separated flow phenomena, for example, laminar separation bubbles and large-scale cove flow separation; 3) confluent boundary-layer flow; 4) boundary-layer and wake development in pressure gradients and with streamline curvature; 5) boundary-layer relaminarization; and 6) multiple wake interactions.

It is apparent that the reliable prediction of the performance of a multi-element airfoil using computational fluid dynamics (CFD) will require accurate modeling of the relevant viscous flow interactions. Our limited understanding is readily apparent on inspection of the results from the recent blind CFD challenge for flow over a two-dimensional three-element airfoil reported by Klausmeyer and Lin.[2] In our view, the numerous and significant disparities between the CFD and the experiment exhibited by this competition serve to illustrate just how far we really are from the goal of having a reliable CFD-based high-lift design tool. The development of such tools for high-lift system aerodynamic performance prediction will require increased attention to fundamental flowfield physics issues.

The focus of this paper is on one particular aspect of a high-lift system flowfield; the confluent boundary layer. The confluent boundary layer is a complex flow that combines certain characteristics of both the classic turbulent boundary layer and wake in a single integrated viscous layer. We first qualitatively describe the confluent boundary layer and introduce some appropriate terminology. Figure 1a is a qualitative sketch of the mean velocity profile prior to any significant confluence between the viscous wall layer and wake. In this case, the wall layer remains distinct from the wake as evidenced by a region of uniform potential flow at the external flow speed U_e that appears between the two viscous layers. The wake centerline is well defined as are the inner and outer wake shear layers. Figure 1b presents a confluent boundary-layer profile after onset of mixing between the wall layer and slat wake. The region of irrotational flow between the wall layer and lower wake shear layer is now gone. The lower wake shear layer is still apparent as a region where the velocity defect $(U_e - \bar{U})$ increases with increasing distance from the wall. The location where $d\bar{U}/dz = 0$ just above the wall has a local velocity $\bar{U} < U_e$ indicating that the wake and wall layer have begun to merge. Although it is tempting to define this as a boundary between the wall layer and lower wake shear layer, this is artificial inasmuch as there is undoubtedly a significant dynamic interaction between the two. In Fig. 1c, the lower wake shear layer has nearly lost its identity and local values of $d\bar{U}/dz$ are small throughout due to the mixing that has occurred with the wall layer. In Fig. 1d, the mixing between the slat wake and wall layer is sufficiently strong that the velocity defect now decreases continuously with distance from the wall. We shall refer to streamwise

Received 18 November 1998; revision received 15 November 1999; accepted for publication 17 November 1999.

*Professor, Hessert Center for Aerospace Research.
†Graduate Research Assistant, Hessert Center for Aerospace Research.

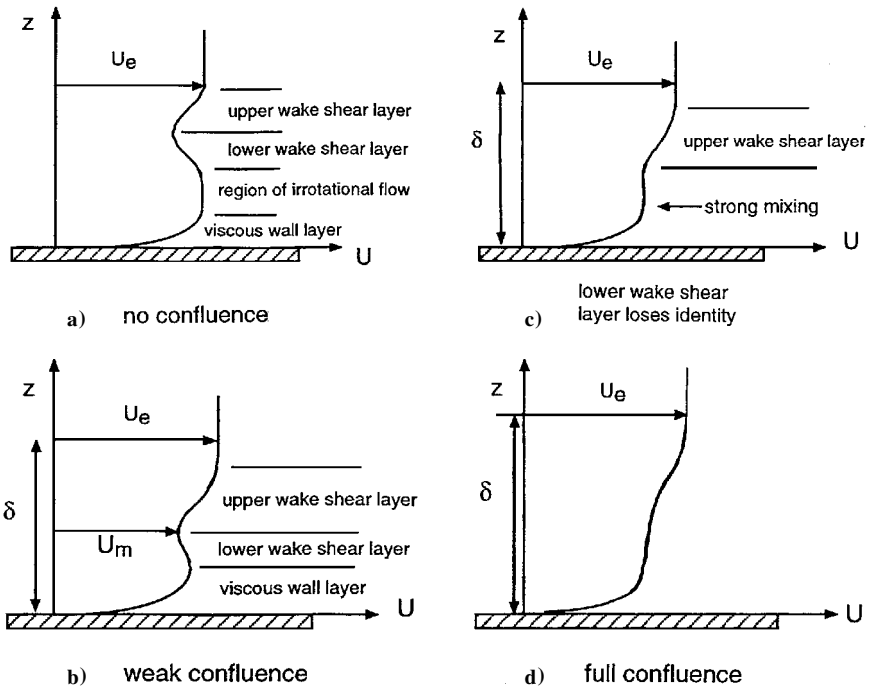

Fig. 1 Schematic of the confluent boundary layer.

regions for which the mean profiles resemble Fig. 1b as associated with weak confluence. Those regions for which the profiles are monotonic, like Fig. 1d, will be referred to as associated with full confluence.

Previous studies involving confluent boundary layers generally fall into two rather broad categories. First, there have been studies on specific two-dimensional high-lift configuration models in both low-speed and pressure tunnels. These studies have typically been carried out as part of a high-lift system configuration optimization and performance testing program (e.g., Nakayama et al.,[3] Mack and McMasters,[4] and Chin et al.[5]). As such, the focus is often not on the confluent layer itself but rather the resulting integrated aerodynamic forces. Measurements of the confluent boundary-layer structure are typically restricted to pitot probe surveys that provide single component mean velocity profiles.

More fundamental studies of confluent boundary layers have been performed, albeit in less realistic geometries. For example, Bario et al.[6] used a tandem arrangement of symmetric airfoils to investigate the interaction between the wake of the upstream airfoil with the boundary layer on the downstream airfoil. In addition, an extensive set of experimental results for confluent boundary layers are reported in a series of papers by the group at Cambridge University: Zhou and Squire,[7,8] Agoropoulos and Squire,[9] and Moghadam and Squire.[10] In these studies, wakes generated by both a flat plate and symmetric airfoils were allowed to merge with the turbulent boundary layer on the floor of a wind tunnel. In each case either a porous top wind-tunnel wall or a contoured insert was used to impose an adverse pressure gradient on the confluent layer. In the adverse pressure gradient cases, the merging of the two viscous layers was accelerated. In those cases where there was strong vortex shedding from the wake generating airfoil, the mixing in the interacting flow was found to be quite strong. The study by Moghadam and Squire[10] involved a swept airfoil and addressed the effects of wake three dimensionality on the confluent boundary-layer structure. Tulapurkara et al.[11] investigated the interaction of both an airfoil and bluff-body wake with a flat plate boundary layer. The higher turbulent fluctuations in the bluff-body wake gave rise to a more rapid mixing and earlier development of a monotonic mean velocity profile. The interaction between a symmetric airfoil wake and flat plate boundary layer as well as between two symmetric airfoils in a wing/leading-edge slat configuration was undertaken by Johnston and Horton.[12] Measurement of confluent boundary-layer development in a very realistic geometry was performed at Lockheed Corporation by Braden et al.[13] using a NASA GAW-1 main element airfoil equipped with a single-slotted trailing flap and a leading-edge slat. Particular emphasis was placed on documenting confluent boundary-layer separation characteristics. A study of the confluent boundary layer on a four-element high-lift system model was performed by Brune and Sikavi[14] at the Boeing Research Wind Tunnel Facility. They used X-wire probes to characterize both the mean and turbulent flow development under conditions representative of takeoff.

This paper describes a fundamental experimental investigation of the confluent boundary layer generated by the interaction of a leading-edge slat wake with the boundary layer on the main element of a two-dimensional multi-element airfoil model. The experiments are performed in both a geometry and pressure gradient environment that is similar to that encountered in actual high-lift systems. The research reported in this paper is performed in an attempt to investigate the flow physics of the confluent boundary layer and to build an archival database on the interaction of the slat wake with the main element wall layer. In addition, an attempt is made to identify clearly the role that slat wake/airfoil boundary-layer confluence plays on lift production and how this influence occurs. To form a comprehensive database for future CFD/turbulence modeling efforts, nonintrusive flowfield surveys were performed for several positions of the slat with respect to the main element. Space limitations prevent presentation of the complete results. Instead, this paper will contrast two cases representing examples of delayed and early wake/boundary-layer confluence.

II. Experimental Facility and Measurement Apparatus

The experiments were performed in an in-draft wind-tunnel facility located at the Hessert Center for Aerospace Research at the University of Notre Dame. Ambient air is drawn through a contraction with inlet area of 2.74×2.74 m and contraction ratio of 20.25:1. The test section is 1.83 m in length, 0.61 m in height, and 0.61 m in width. To facilitate flow visualization and laser Doppler velocimetry (LDV), one sidewall of the test section is made of glass.

A schematic of the high-lift system model is shown in Fig. 2. The model is a simplified two-dimensional multi-element airfoil, the main element of which is elliptical with a maximum thickness-to-chord ratio of 15%. A plain tapered flap of 30% chord length was hinged at the trailing edge to provide the same characteristic

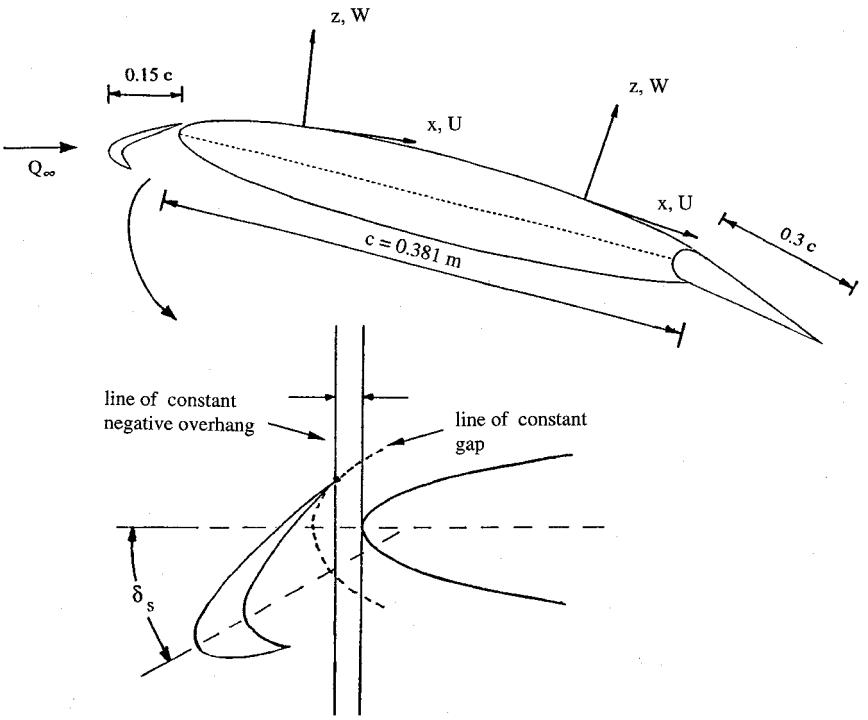

Fig. 2 Schematic of the multi-element airfoil model.

peaked main element pressure distribution for confluent boundary-layer development that occurs in actual high-lift systems. A leading-edge slat, the upper surface of which takes the shape of the leading edge of the main airfoil, was deployed in front of the main element. The slat has a lower surface cove region that is virtually identical to that of the often studied McDonnell Douglas three-element high-lift system.[2] The position of the slat relative to the main element was fully adjustable in terms of angle of attack, gap, and overhang. For readers unfamiliar with slat rigging nomenclature, Fig. 2 also shows representative lines of constant slat gap and overhang. The coordinate system that is used in presenting the measurements is also shown in Fig. 2. As indicated, x is the spatial coordinate locally tangent to the main element surface with the corresponding local tangential velocity component U. The spatial coordinate locally normal to the main element is z, with corresponding local normal velocity component W.

Unless otherwise noted, the experiments were performed at a stowed chord Reynolds number of nominally 1.2×10^6.

To facilitate flow visualization of the slat wake–main element boundary-layer confluence, both the main element and the leading-edge slat contained separate internal plenums connected to surface smoke injection slits. A kerosene smoke generator was connected via flexible tubing to both internal plenums. The slit on the main element allowed the seepage of smoke into the boundary layer near the stagnation point (which was nominally located on the lower surface). The slit on the top surface of the leading-edge slat allowed seepage of smoke into the slat boundary layer and thereby provided a means of visualizing the slat wake. An argon-ion laser light sheet was positioned in the x–z centerspan plane of the model to illuminate the smoke and thereby visualize a slice of the confluent boundary layer. To obtain integrated lift, a second identical multi-element airfoil model was constructed that contained numerous static pressure taps on the upper and lower surfaces of the slat, main element, and trailing flap. Both multi-element airfoil models nearly spanned the test section and were installed in the wind tunnel with transparent end plates. Spanwise arrays of airfoil pressure taps and supporting flow surveys confirmed that the flow over the model was two dimensional. The observed spanwise variation of mean flow velocity at any given fixed chordwise location was always less than 1%.

Transition was allowed to occur naturally inasmuch as no surface grit or boundary layer trips were used. However, LDV measurements indicate the boundary layer on the main element to be turbulent by the first chordwise measurement station, which was $x/c = 0.06$. Hot-wire surveys indicated the boundary layer on the slat top surface just upstream of the trailing edge to be transitional. Smoke flow visualization revealed the flow in the slat cove region to be separated. Hot-wire measurements made immediately downstream of the slat trailing edge indicate the near wake to be in a transitional state with most fluctuation energy residing in discrete spectral modes associated with vortex shedding from the slat. The importance of the assumed slat boundary-layer transition state and location on CFD prediction of high-lift flows was recently discussed in the paper by Rumsey et al.[15]

The structure of the confluent boundary layer was investigated nonintrusively by means of two-component LDV surveys at selected chordwise locations on the main element. The measurement location was at the center span of the model. An Aerometrics three-component, fiber optic LDV system was operated in two-component, coincident, backscatter mode using a 5-W argon-ion laser. Frequency shifting was used to unambiguously resolve flow direction. Results for both mean flow and turbulence quantities represent ensemble averages over at least 10,000 valid coincident burst events. An Aerometrics seed particle generator using a mixture of propylene glycol and distilled water was used to seed the flow near the tunnel inlet with droplets that are nominally in the 1–2 μm range. The transceiver of the LDV system was mounted to a computer-controlled traverse table. The 514- and 488-nm laser wavelengths were used to measure the U and W velocity components, respectively. The diameter of the LDV measurement volume, which is the limiting factor in setting the spatial resolution in the z coordinate, is 239 μm.

An error analysis including the effects of both bias and precision errors showed that the uncertainty in the measured mean velocity is ± 0.17 m/s within 95% confidence. For the streamwise component this translates to a relative error with respect to the external freestream of $\pm 0.56\%$. The uncertainty for the local values of the normal stresses was computed to be $\pm 1.4\%$, again within the 95% confidence interval. The corresponding values for the measured Reynolds stresses are in the range of $\pm 4\%$.

III. Experimental Results

A. Summary of Flow Visualization and Integrated Lift Results

The focus of the experiments is on the characterization of the structure and development of the slat wake/main element confluent

boundary layer and the role that confluence plays on lift production in high-lift systems. For this reason, the geometric angle of attack and trailing-edge flap deflection were held fixed in the experiments while the leading-edge slat gap and overhang were then varied over a range of positions. It was found that a main element geometric angle of attack of 10 deg and a trailing-edge flap deflection of 13 deg represented a good compromise in terms of producing a surface pressure distribution on the model similar to those encountered in actual high-lift systems while minimizing the effects of wind-tunnel blockage. The slat was positioned at an attack angle of −10 deg so that it faced directly into the approach flow.

Even at the main element angle of attack quoted earlier, however, the tunnel blockage was still 15%. To assess the effect of blockage, experiments were also performed in a larger in-draft tunnel at the Hessert Center with a 1.52 × 1.52 m cross-sectional area for which the blockage was only 2.4%. It was found that standard blockage corrections applied to the data obtained in the smaller test section yielded results matching those obtained in the larger tunnel. Perhaps most important for the purposes of this investigation, however, was the observation that integrated lift coefficients showed the same trends with variation in slat gap and overhang in both facilities. Because our purpose was simply to provide a realistic pressure gradient environment for the confluent boundary layer to develop and not to produce lift data for extrapolation to flight, the blockage issue was not a significant factor. The higher overall flow quality of the smaller tunnel motivated its use in this study.

To further reduce the parameter space for detailed LDV study, integrated lift and confluent boundary-layer flow visualization was first performed for a variety of slat overhang and gap settings. The resulting variation of lift coefficient (based on integration of measured surface pressure distributions) with slat position is shown in Fig. 3. In Fig. 3 the integrated lift coefficient is $C_{l\text{total}}$ and is normalized by the lift coefficient obtained with the slat fully stowed, C_{l0}. This normalization shows the relative change in lift coefficient with slat gap and overhang variation. In Fig. 3, the lift measurements are presented as shaded contours in slat gap–overhang parameter space. Both the slat gap and overhang are expressed as percentages of the stowed chord length. The range of gap and overhang values shown in Fig. 3 span those typically encountered in high-lift systems. Lighter shading indicates the highest relative lift coefficient. Note that optimum lift is obtained for a quite narrow range of slat gap and that lift falls off for both larger and smaller slat gap settings. Figure 3 shows that the lift also falls off with negative overhang. These data show what has often been observed in design tests of multi-element airfoils: The performance of the high-lift system can be quite sensitive to slat position relative to the main element. With the indicated sensitivity, it is not surprising that a slat orientation that is found to be optimum in ground tests may not be optimum at flight Reynolds numbers. This has been a well-known problem in the design of high-lift systems for commercial transports. Note that much of the early high-lift system development work at Boeing prior to the 757-200 model was performed at stowed chord Reynolds numbers of 1×10^6 (comparable to this study) in the University of Washington Aeronautical Laboratories.

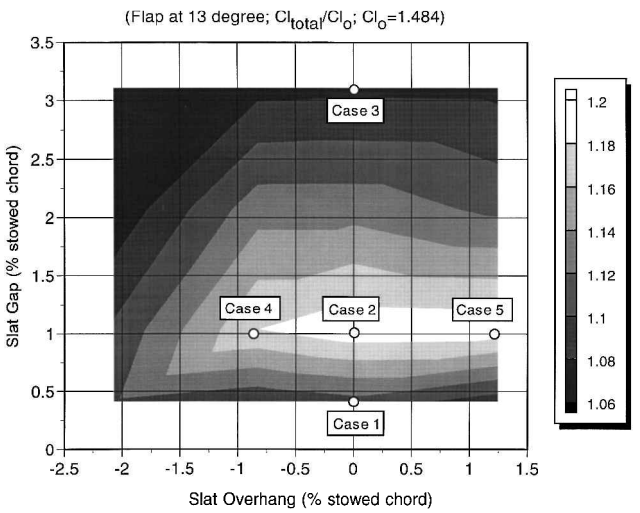

Fig. 3 Lift coefficient contours in slat gap-overhang parameter space.

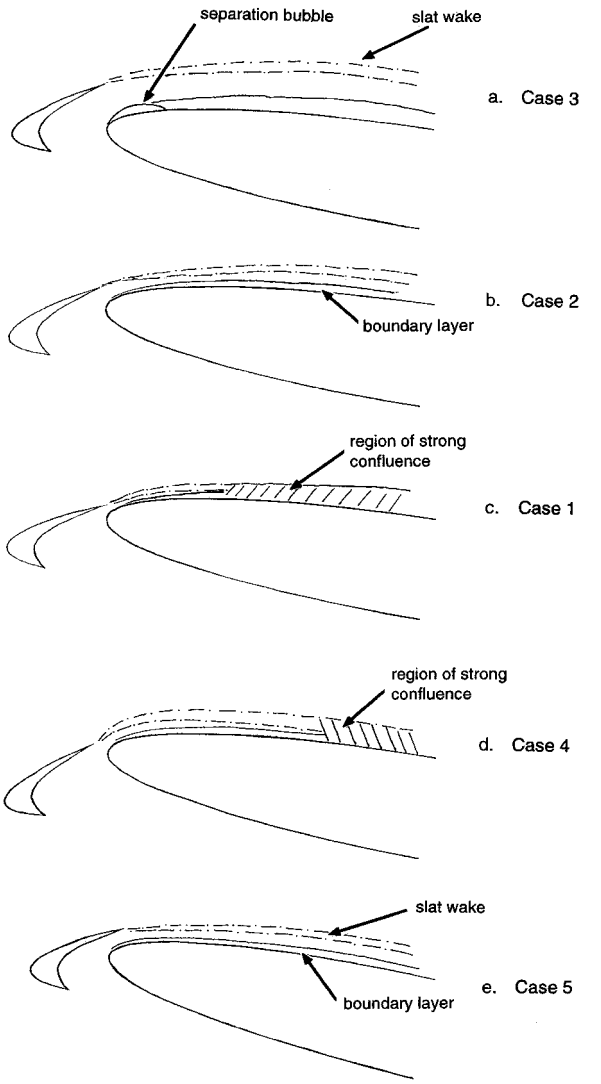

Fig. 4 Summary of flow visualization results.

To clarify the role of the leading-edge confluent boundary layer on the observed variation in lift, smoke injection flow visualization was performed for several of the slat gap/overhang combinations indicated in Fig. 3, and key results are qualitatively summarized in a series of schematics presented in Fig. 4. Case numbers correspond to those shown in Fig. 3. Figure 4a presents case 3, which corresponds to zero overhang and a slat gap of 3.1% stowed chord. At this comparatively large slat gap setting, surface pressure measurements (not presented) show that the slat is unloaded and is, therefore, ineffective at moderating the surface pressure on the leading edge of the main element. As a consequence, a large separation bubble is observed to form on the main element and lift is reduced. Figure 4b presents case 2, which corresponds to zero overhang and a 1% gap setting. This configuration is nearly optimum in terms of lift production. Surface pressure measurements indicate the slat is highly loaded. The flow visualization shows the slat wake and boundary layer remain separate entities, and strong confluence is apparently delayed until the most aft chordwise stations. Figure 4c presents case 1, which corresponds to zero overhang and 0.4% gap setting. This case represents the smallest slat gap investigated. Although pressure measurements indicate that the slat remains loaded, Fig. 4c suggests a more rapid merging of the slat wake and main element boundary layer near the leading edge. Associated with this forced early confluence, the lift

production is adversely affected. Figure 4d corresponds to case 4, which has the same gap setting as in case 2 but a negative overhang of −0.83%. In this case, pressure measurements indicate that the slat is not highly loaded, and the flow visualization indicates a vertical jetting of the wake near the trailing edge. The main element boundary layer, while remaining attached, grows in a strong adverse pressure gradient environment. Strong confluence is observed upstream of the midchord position. Finally, Fig. 4e presents case 5, which corresponds to 1.2% overhang and 1% gap. As in case 2, the slat is highly loaded and moderates the main element leading-edge pressure peak. The slat wake and boundary-layer confluence is delayed until well downstream yielding favorable lift behavior.

In summary, Fig. 4 shows that optimum lift behavior appears associated with cases for which strong slat wake/main element boundary-layer confluence is delayed to aft chordwise stations. Note that case 3 simply corresponds to a case in which confluence is not the key issue, but rather, the slat is ineffective at moderating the main element pressure peak due to the large gap setting.

Of course, the primary benefit of a slat is to increase the main element attack angle before separation occurs and thereby increase $C_{L\max}$. However, inasmuch as the higher lift at constant angle of attack observed in our experiments represents a healthier main element boundary layer, it can be presumed that higher $C_{L\max}$ would result.

B. Confluent Boundary-Layer LDV Flowfield Surveys

Detailed two-component LDV surveys of the confluent boundary layer were performed for a variety of the slat gap and overhang settings shown in Fig. 3. Here we focus on a comparison of confluent boundary-layer flowfield surveys for case 2, which corresponds to a near-optimum slat setting, and case 1, which involves an early onset of strong confluence due to the reduced gap setting. In presenting the LDV measurements we will first discuss the mean flow development, followed in turn by the presentation of turbulence quantities.

1. Mean Flow Development in the Confluent Layer

Figure 5 compares mean velocity profiles, $U(z)/U_e$ for cases 1 and 2 as obtained at several chordwise locations on the main element. U_e is the local velocity outside the viscous layer and is of course a function of x/c. At $x/c = 0.1$, the slat wake is well defined for both cases. The wake and viscous wall layer are well separated at this chordwise location for case 2. In case 1, however, mixing between the wake and boundary layer has already commenced at $x/c = 0.1$ and is well underway by $x/c = 0.3$. As a consequence, the case 1 flow is more severely retarded near the wall in relation to case 2. This trend is observed to continue for each x/c location investigated and is associated with the early onset of confluence between the slat wake and boundary layer. Figure 5 shows evidence of onset of very weak confluence for case 2 at the $x/c = 0.3$ location. Figure 5 suggests an accelerated and more aggressive mixing between the slat wake and main element boundary layer for case 1.

Figure 5 serves to illustrate another interesting difference between the mean flow data of cases 1 and 2. Each datum point in Fig. 5 is based on an ensemble average over at least 10,000 valid LDV burst events. As a result, the case 2 profiles are quite smooth and exhibit very little scatter. In contrast, despite the long effective averaging times used for the measurements, the case 1 profiles of Fig. 5 show considerable scatter, especially in the wake region. It was found that this scatter could not be removed by repeating the measurements with even longer averaging times. Velocity histograms (not presented here) revealed a bimodal character for case 1 that suggested an unsteady or mode switching type of behavior. This bimodal behavior was most apparent in the W-component histograms. The origin was traced to unsteady separated flow behavior in the slat cove. This unsteady aspect of the high-lift flowfield, and the associated acoustic emission, is the topic of a detailed investigation using a fully instrumented slat, the results of which will be reported in a separate paper. To the authors' knowledge, the unsteady aspects of high-lift flows have not received attention in the past.

Despite the obvious differences between the confluent boundary-layer mean velocity profiles shown in Fig. 5 and those of conventional turbulent boundary layers, note that, in each case, sufficiently close to the wall the profiles exhibit classic log law-of-the-wall scaling behavior. This may be seen in Fig. 6, which presents selected case 2 mean velocity profiles plotted in inner wall variables, $u^+ = U/u_\tau$ and $z^+ = (zu_\tau)/\nu$, where u_τ is the local friction velocity and ν is the kinematic viscosity. Figure 6 shows log law behavior in each case for $z^+ < 200$. Note that the profiles have been biased from each other by $\Delta u^+ = 2$ for the purpose of facilitating their comparison in a single figure. To apply inner variable scaling, the local skin friction was measured by both the Clauser and Preston tube methods,

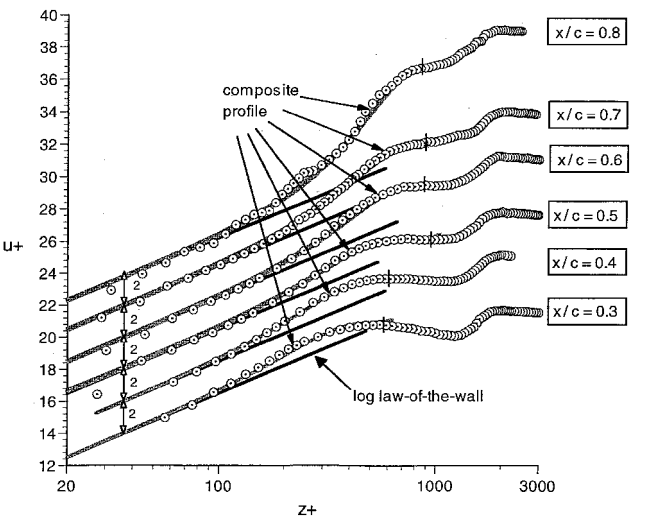

Fig. 6 Inner variable scaling of case 2 mean velocity profiles.

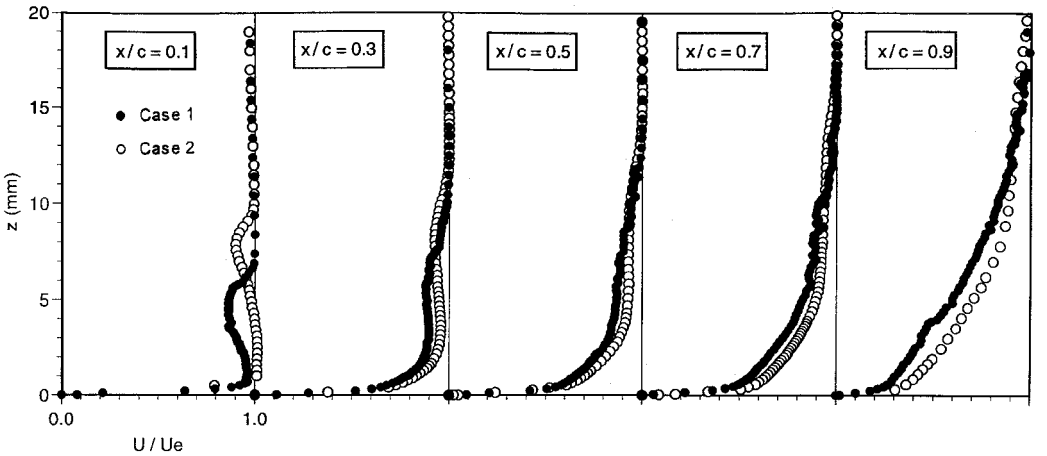

Fig. 5 Comparison of mean velocity profiles for cases 1 and 2.

which gave quite similar results. Although both these methods assume log law behavior, plots of U/U_e vs $\ln(U_e z/\nu)$ exhibited a well-defined logarithmic zone, and subsequent inner variable scaling of the profiles using the experimentally obtained values of skin friction did indeed yield profiles of the form $u^+ = (1/\kappa)\ln z^+ + B$, with $\kappa = 0.41$ and $B = 5$ (this line is indicated in Fig. 6).

For z locations extending from the wall to the lower edge of the slat wake, it was found that the profiles are well represented by a modified form of Coles' composite relation:

$$u^+ = (1/\kappa)\ln z^+ + B + [\Pi_*(x, \delta_w)/\kappa]\left[2\sin^2(\pi z/2\delta_w)\right] \quad (1)$$

In Eq. (1), $\Pi_*(x, \delta_w)$ is a wake parameter that at a given x location is given by

$$\Pi_*(\delta_w) = (\kappa/2)\left[U_w^+ - (1/\kappa)\ln\left(\delta_w^+\right) - B\right] \quad (2)$$

where δ_w is the distance from the wall to the lower edge of the slat wake, δ_w^+ is the corresponding value in wall units, and $U_w^+ = U_w/u_\tau$ is the corresponding velocity at the lower edge of the wake. The fit of Eq. (1) to the case 2 mean velocity data is shown in Fig. 6 and is denoted by the term composite profile. The z^+ limit of the fit at each x/c is denoted by a small vertical line. This ranges from 600 wall units at forward positions on the main element to nearly 1000 wall units for the aftmost chordwise stations.

For x/c locations upstream of full confluence, it was found that the value of δ_w that provides the best composite scaling of the mean velocity measurements corresponds to the local z value where $\overline{u'w'} = 0$ above the wall. Note that this is not the same z location where $d\bar{U}/dz = 0$; this occurs farther from the wall. This aspect will be discussed further on presentation of the Reynolds stress measurements in the following section. For those chordwise stations corresponding to full confluence, there is no near-wall location where either $\overline{u'w'}$ or $d\bar{U}/dz$ equals zero. For such locations the length scale δ_w cannot be associated with any readily identifiable feature of the profiles of either mean flow or turbulence quantities. However, it was found in each case that δ_w varied exponentially with x/c. Extrapolation of the exponential fit of the values of $\delta_w(x)$ as determined upstream of full confluence by the $\overline{u'w'} = 0$ condition provided an excellent representation of the optimum values of δ_w in the region of full confluence. In this region, it is always true that δ_w was located below the Reynolds stress minimum.

Although not presented in this paper, inner variable scaling of mean velocity profiles for case 1 using the composite relation (1) also provided a very satisfactory fit below the slat wake extending to $z^+ = 500, \ldots, 600$. For case 1, it was found that the increased scatter of the profiles associated with unsteady effects is confined primarily to the wake region whereas the near-wall region appears largely unaffected.

Focusing on the outermost portion of the confluent layer, Fig. 7 shows the non-dimensional wake velocity defect, $(\bar{U} - \bar{U}_m)/(\bar{U}_e - \bar{U}_m)$, in the upper wake shear layer for case 2 as a function of $\eta = (z - z_*)/\delta_\Omega$. $\bar{U}_m$ is the minimum velocity in the wake, the location z_* corresponds to the center of the outer wake shear layer, that is the location where $\bar{U} = \frac{1}{2}(U_e + \bar{U}_m)$, and δ_Ω is the upper wake shear layer vorticity thickness. Figure 7 shows that despite the strong adverse pressure gradient environment in which the flow develops, the outermost portion of the confluent boundary-layer mean velocity exhibits approximate similarity behavior when scaled in the manner described earlier. The solid curve shown in Fig. 7 is a modified hyperbolic tangent profile of the form

$$(U - U_m)/(U_e - U_m) = 0.5(1 + \tanh(\eta)\{1 + \operatorname{sech}^2(\eta)[0.05\tanh(\eta) - 0.23]\}) \quad (3)$$

The term in brackets contains both symmetric and antisymmetric corrections to a basic hyperbolic tangent profile. The collapse shown in Fig. 7 is perhaps not surprising given the analysis by Townsend,[16] which demonstrates that a low-momentum deficit wake can admit to approximate similarity solutions even in a pressure gradient environment. Similar scaling results were also obtained for the outer wake shear layer of case 1.

The scaling embodied by Eq. (3) was was not suitable for describing the inner wake shear layer. For locations above the wall corresponding to $0.2 < z/\delta < 0.5$ (here δ is the distance from the wall to the location where $\bar{U} = 0.99U_e$), there is little hope of similarity scaling due to the very strong streamwise variation in the profile shape. This comes about as a consequence of the strong mixing with the main element wall layer.

Velocity defect scaling may be employed to document the development of the confluent boundary layer, and the results for case 2 are presented in Fig. 8. In Fig. 8 the wall normal coordinate z is scaled by δ. Using defect scaling, it is apparent that weak confluence commences near $x/c = 0.2$ as evidenced by a nonzero defect below the wake. Note that the profiles exhibit reasonable collapse for $z/\delta > 0.65$, consistent with the preceding discussion of the outer wake shear layer. Below this region, the defect grows with streamwise distance. For a conventional turbulent boundary layer, the momentum defect decreases monotonically with z/δ. For the confluent boundary layer shown in Fig. 8, locations above the wall for which the velocity defect increases are evidence that the slat wake has not fully mixed with the boundary layer and maintains some semblance of a separate identity, that is, the confluence is weak. Based on Fig. 8, this would suggest that, for case 2, full or strong confluence is reached by approximately $x/c = 0.7$. Note that downstream of this location, the profiles exhibit large changes in character with the defect near the wall growing very rapidly. As one might expect, velocity defect scaling of the case 1 mean velocity profiles (not presented) reveal that the slat wake and boundary layer have begun to merge upstream of $x/c = 0.1$ and appear completely mixed by $x/c = 0.4$ as evidenced by a continuous decrease in velocity defect with z.

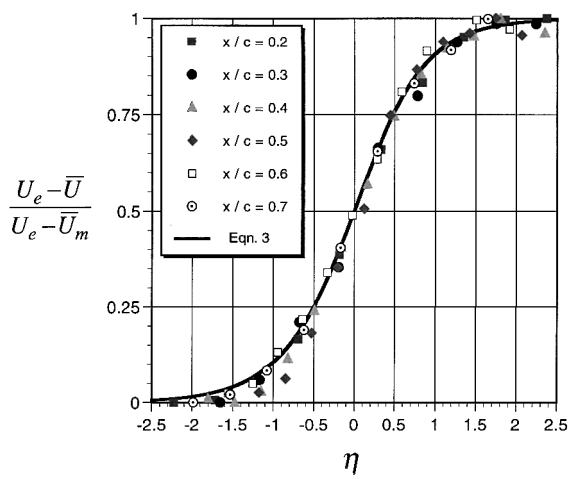

Fig. 7 Scaled upper wake shear layer profiles for case 2.

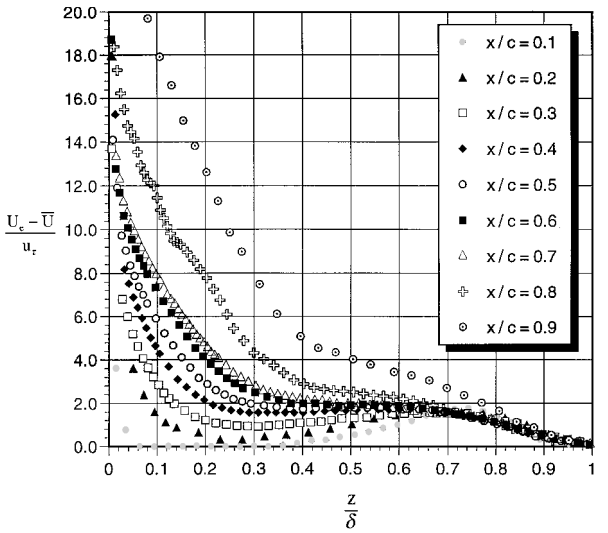

Fig. 8 Velocity defect scaling for case 2.

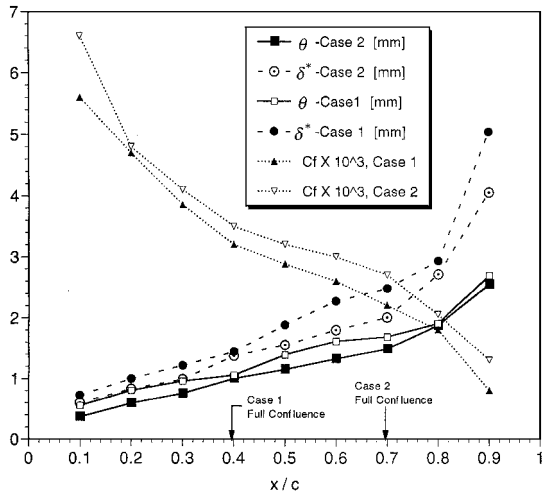

Fig. 9a Streamwise variation in integral thickness parameters and skin friction.

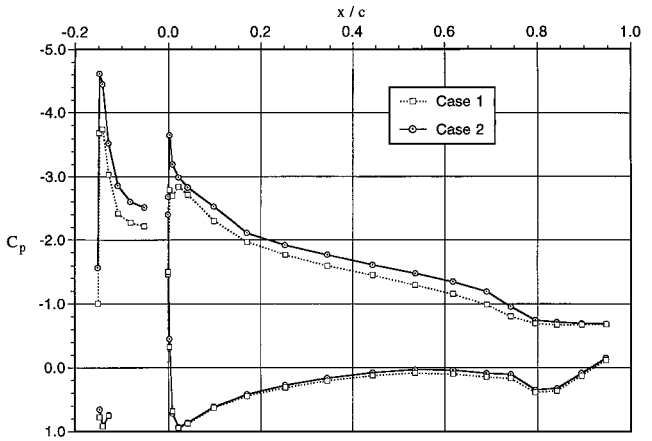

Fig. 9b Comparison of case 1 and 2 pressure distributions.

A comparison of the streamwise variation of the displacement and momentum thicknesses for cases 1 and 2 is presented in Fig. 9a. Figure 9a is derived from numerical integration of mean flow profiles like those presented in Fig. 5. The integration is from the wall to the inviscid freestream and so includes the entire viscous layer. Figure 9a shows that at each chordwise station the case 1 displacement thickness exceeds that for case 2. This is consistent with the case 1 flow mixing more aggressively with the slat wake and being more severely retarded in relation to its case 2 counterpart. Because of the associated streamline displacement effect, the suction pressure on the main element is reduced, as is shown from the comparison of the cases 1 and 2 pressure distributions shown in Fig. 9b. Hence, even in the absence of separation, lift is adversely affected by the confluence. Figure 9a also indicates the streamwise locations of full confluence based on the defect scaling described earlier. Note that both cases' 1 and 2 displacement thickness show a significant increase in growth rate starting at these locations. Figure 9a also presents the streamwise variation in the skin-friction coefficient for each case.

2. Development of Turbulence Quantities in the Confluent Layer

Figure 10a presents profiles of the local tangential and normal-component turbulence intensities as obtained at selected chordwise locations on the main element for case 2. At each z location, $\sqrt{u'^2}/U_e > \sqrt{w'^2}/U_e$ as expected because the Reynolds stress working against the mean velocity gradient will feed energy into the tangential u' fluctuating component first. Outside the viscous layer, the u' and w' intensities are approximately equal, which is consistent with a background turbulence in the wind tunnel that is nearly isotropic. At each chordwise station shown, peak u' intensity occurs very near the wall at a value of approximately 10%, which is typical of turbulent boundary layers in general. Peak near-wall w' intensity values are between 4 and 5%. In contrast, the u'- and w'-component turbulence intensities for $0.3 < z/\delta < 0.9$, which the mean velocity profiles indicate to be associated with the slat wake, are observed to decay with x/c. This is associated with the reduction in mean shear as the slat wake widens. There is streamwise growth in the u'- and w'-component intensities for $0.09 < z/\delta < 0.3$, particularly near $x/c = 0.6$–0.7, which is the streamwise location associated with the onset of full confluence between the wake and wall region.

Figure 10b presents sample u' and w' intensity profiles for case 1. One difference between these data and the corresponding measurements for case 2 is that the u' intensity near the wall is considerably higher at small x/c for case 1. Note that the abscissa scale for the intensity profiles at $x/c = 0.2$ is different than the others to accommodate the higher near-wall intensities. With increased x/c, the case 1 wall layer intensity appears to relax toward similar values as occurred in case 2. Measurements near the main element leading edge and slat trailing edge suggest that the high-turbulence levels near the wall originate from the interaction of the lower slat wake shear layer with the wall layer on the main element as a consequence of the reduced slat gap setting. The case 1 turbulence intensity values for z/δ corresponding to the wake region are observed to decay initially, as in case 2. However, unlike case 2, the fluctuation level in the outer wake exhibits renewed growth downstream of $x/c = 0.4$. This indicates a more complex and dynamically active wake structure than occurred for case 2. As in case 2, there is growth in the turbulence level for regions of z/δ corresponding to the region of mixing between the wall layer and slat wake.

Figure 11 presents the streamwise evolution of the nondimensional Reynolds stress $-\overline{uw}/U_e^2$ for case 2. The z variation of the Reynolds stress across the confluent boundary layer can be characterized by three distinct regions. In the region nearest the wall, $-\overline{uw} > 0$. With sufficient distance above the wall, the Reynolds stress changes sign and becomes negative in the lower slat wake shear layer. A second change in sign occurs as the Reynolds stress becomes positive again in the top slat wake shear layer. The locus of points corresponding to z locations where $-\overline{uw} = 0$ closest to the wall is shown by a dashed line in Fig. 11. As discussed earlier, for streamwise locations upstream of the onset of full confluence ($x/c = 0.7$), these z locations coincide with the scaling length δ_w in Eq. (1). The solid curve shown in Fig. 11 is the locus of points corresponding to where $\partial\bar{U}/\partial z = 0$ nearest the wall. Note that by $x/c = 0.7$ the lower shear layer of the slat wake and wall layer have mixed such that $\partial\bar{U}/\partial z > 0$ throughout the confluent boundary layer. For z locations between the solid and dashed curves, the turbulence production term $-\overline{uw}\,\partial\bar{U}/\partial z$ is negative. Such countergradient momentum transport violates standard eddy-viscosity-based turbulence models because it requires a negative mixing length. In this experiment, the region of countergradient transport is observed to be restricted to the wall layer/lower slat wake shear layer interface for those chordwise locations upstream of where the slat wake and wall layer have thoroughly mixed. Countergradient transport has been observed in other experiments involving wake/boundary-layer confluence,[7–9] as well as in wall jets and curved turbulent flows near the location of maximum velocity.[17] We have already seen that the mean velocity profile in the region of mixing between the wall layer and wake changes dramatically in the streamwise direction so as to prohibit any type of similarity scaling. In such a region, memory effects associated with streamwise evolution are likely to be very important. This would invalidate a gradient transport model in which Reynolds stress is assumed to depend only on the local strain rate.

Figure 12 presents the streamwise Reynolds stress evolution for the case 1 slat configuration. As in Fig. 11, the dashed and solid curves represent the z locations where $-\overline{uw} = 0$ and where $\partial\bar{U}/\partial z = 0$ below the slat wake shear layer, respectively. In the region between the curves, turbulence production is negative. As a consequence of the forced early confluence in case 1, the $\partial\bar{U}/\partial z = 0$ condition below the slat wake is lost by $x/c = 0.4$. Similarly, the region where $-\overline{uw} < 0$ in the lower slat shear layer disappears much earlier than in case 2.

Because $\overline{u^2} > \overline{w^2}$ (as shown in Fig. 10) and because the confluent layer develops in a strong adverse pressure gradient environment,

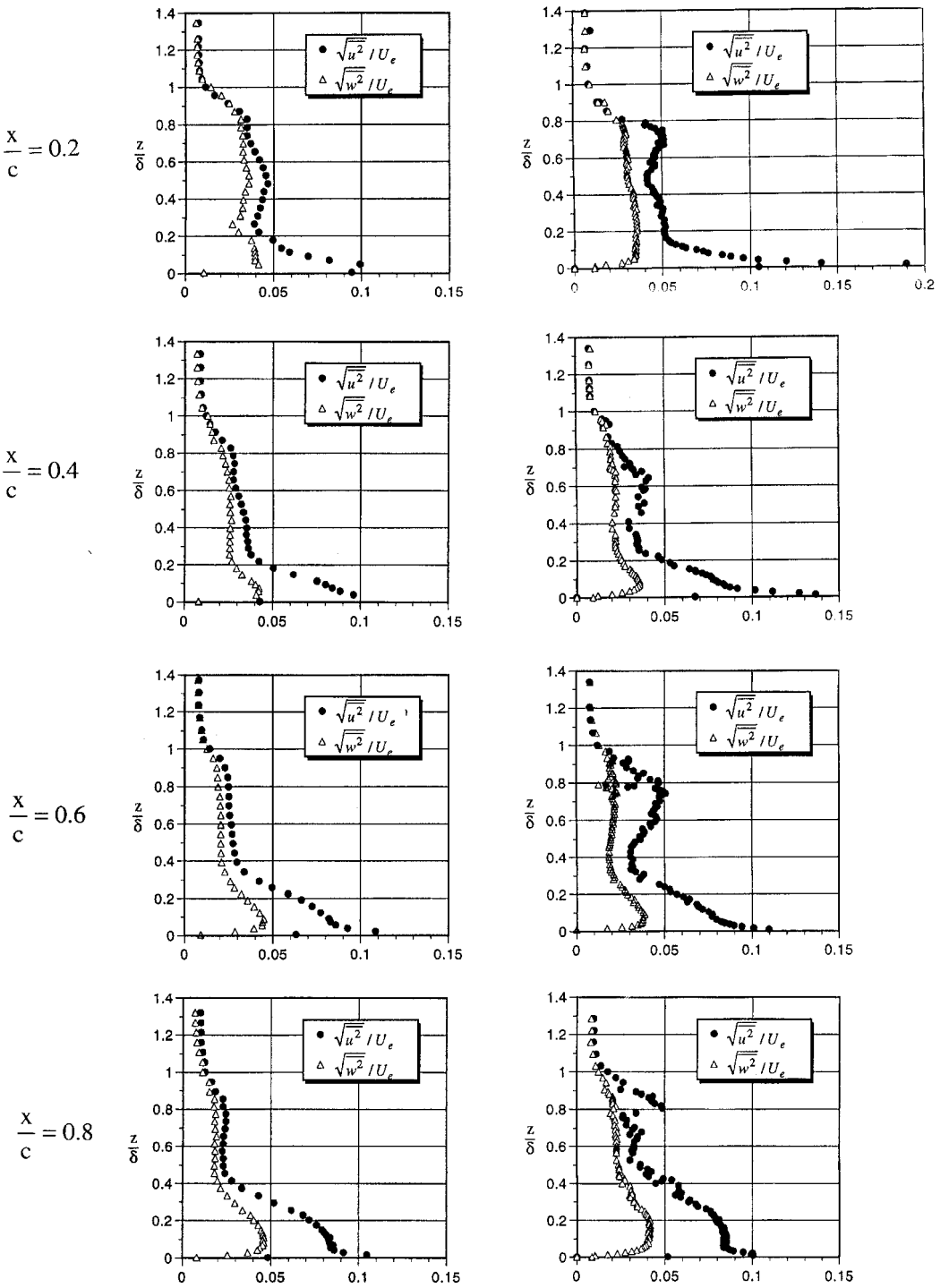

Fig. 10 Profiles of local tangential and normal-component turbulence intensities.

that is, $\partial \bar{U}/\partial x < 0$, the term $-(\overline{u^2} - \overline{w^2})\,\partial \bar{U}/\partial x$ represents an additional dilatational turbulence production mechanism that can augment the shear production term, $-\overline{uw}\,\partial \bar{U}/\partial z$. Figure 13 shows an example comparison of these two production terms at $x/c = 0.6$ for case 2. Note that the turbulence production at the wall greatly exceeds that associated with the wake shear layers. This was also found to be true at the most upstream locations. Figure 13 also shows that shear turbulence production dominates over the dilatational term. That is, despite the strong pressure gradient environment, the main element confluent boundary layer is shear dominated. This was observed at each x/c location for both cases 2 and 1. Note that this may not be the situation in the vicinity of incipient flow separation.

3. Mixing Length Evolution

As described in detail by Wilcox,[18] turbulent flows are often modeled by invoking an eddy viscosity concept that relates the Reynolds stress to the local strain rate. That is,

$$-\overline{uw} = \nu_t \frac{\partial \bar{U}}{\partial z} \tag{4}$$

where ν_t is a kinematic eddy viscosity. In the Prandtl mixing length hypothesis the eddy viscosity is given by

$$\nu_t = \ell_m^2 \frac{\partial \bar{U}}{\partial z} \tag{5}$$

where ℓ_m is a so-called mixing length and, in analogy to the mean free path in the kinetic theory of gases, is related to the cross-stream

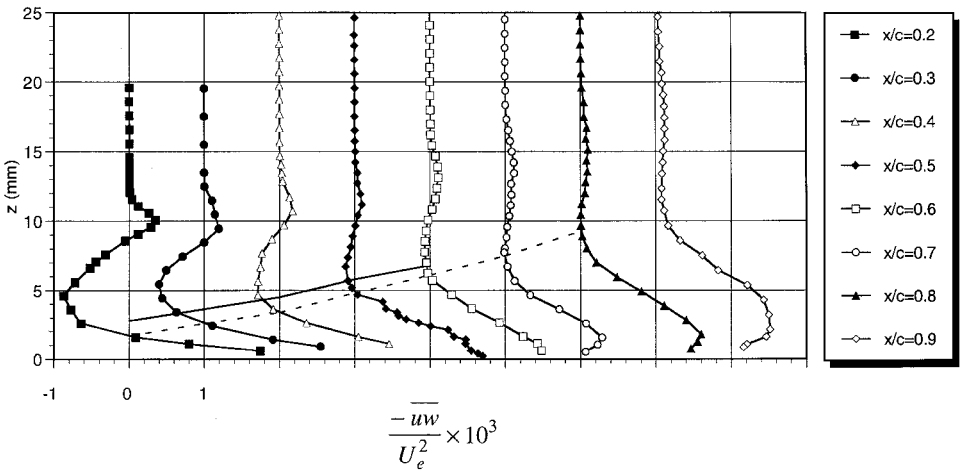

Fig. 11 Streamwise evolution of nondimensional Reynolds stress for case 2.

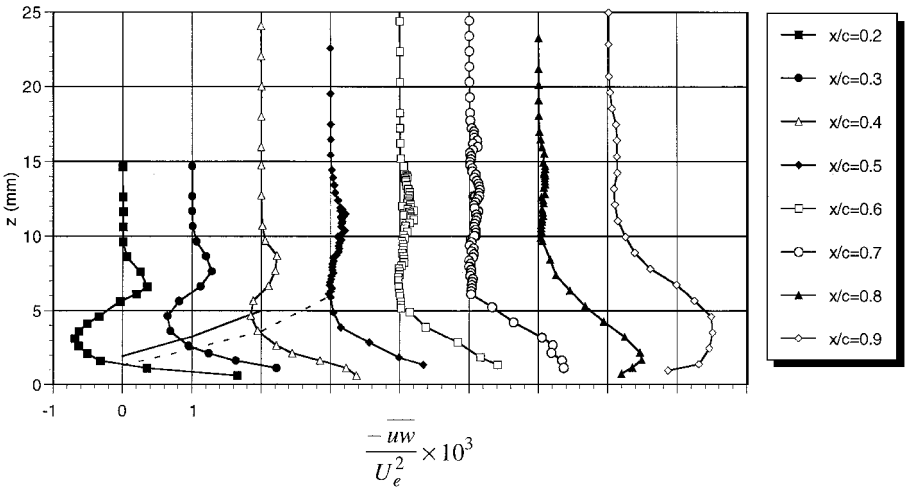

Fig. 12 Streamwise evolution of nondimensional Reynolds stress for case 1.

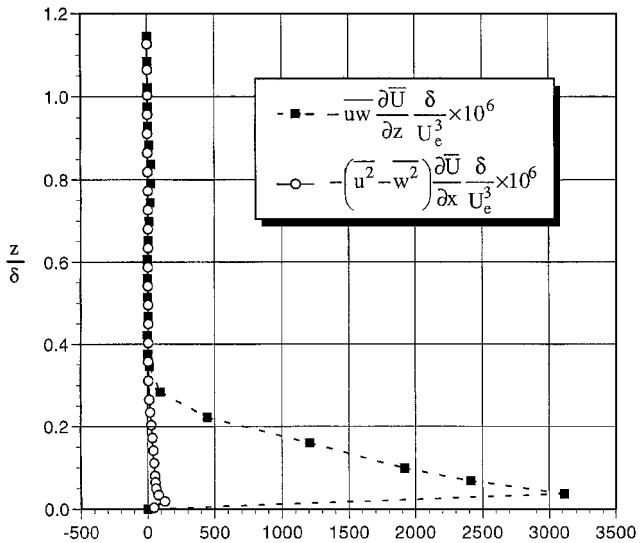

Fig. 13 Turbulence production for case 2 at $x/c = 0.6$.

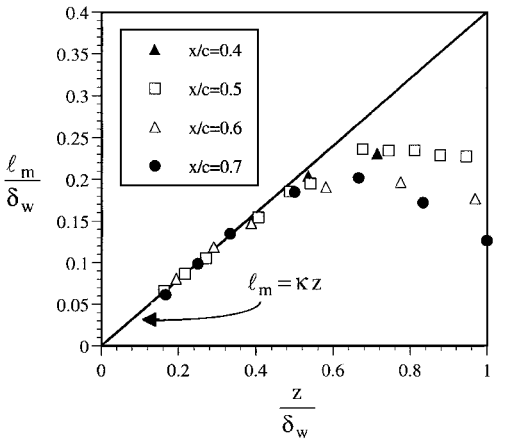

Fig. 14 Profiles of mixing length ℓ_m across the near wall region of the confluent boundary layer for case 2.

distance over which a lump of fluid is transported while preserving its streamwise momentum. There have been numerous criticisms of this analogy. However, irrespective of physical interpretation, the mixing length is a measurable quantity that almost invariably finds its way into Reynolds-averaged Navier–Stokes computations. For this reason we next document the mixing length evolution in the confluent boundary layer.

Using measured profiles of mean velocity and Reynolds stress, the Prandtl mixing length was determined via the relation

$$\ell_m = \left(\frac{-\overline{uw}}{\partial\bar{U}/\partial z|\partial\bar{U}/\partial z|}\right)^{\frac{1}{2}} \tag{6}$$

The observed mixing length variation across the confluent boundary layer may be classified in terms of three distinct regions. In the viscous wall layer, that is, below the lower slat wake shear layer, $z < \delta_w$, the mixing length exhibits behavior that is reminiscent of that encountered in conventional boundary layers. Figure 14 presents sample profiles of the mixing length ℓ_m across the near wall region of the confluent boundary layer. In Fig. 14, both the mixing length and wall normal coordinate are nondimensionalized by the local

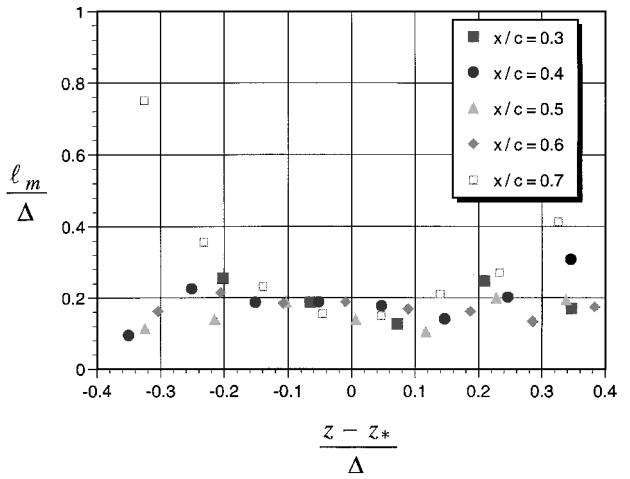

Fig. 15 Profiles of mixing length ℓ_m across the outer wake shear layer for case 2.

length scale δ_w. In this scaling, $z/\delta_w = 1$ corresponds approximately to the lower boundary of the slat wake. Figure 14 shows that in the immediate vicinity of the wall the mixing length is given by $\ell_m = \kappa z$, where κ is the von Kármán constant. This relation, along with the observation that peak near-wall Reynolds stress $-\overline{uw})_{\max}/u_\tau^2 \approx 1$, is fully consistent with the observation of a logarithmic law-of-the-wall mean velocity variation.

As shown in Fig. 14, with sufficient distance above the wall the mixing length departs from its linear variation with z and gradually approaches a relatively constant plateau with most values of $\ell_m/\delta_w \approx 0.19, \ldots, 0.24$. Note that the increased scatter in mixing length values near $z/\delta_w = 1$ is because the mean strain rate $\partial\bar{U}/\partial z \to 0$ in this region of mixing between the wake and wall layer.

As already described, the interface between the lower slat wake shear layer and wall layer is characterized by countergradient momentum transport, and the mixing length is, therefore, undefined there. This effect is greatest in the initial stages of confluence between the wall layer and wake as documented in Figs. 11 and 12. Even farther downstream, where the wake and wall layer have undergone considerable mixing, it is difficult to obtain reliable mixing length values because the mean strain rate, $\partial\bar{U}/\partial z$, is quite small due to the considerable mixing that occurs in this region.

Figure 15 presents the mixing lengths in the outer wake shear layer as obtained at several chordwise locations. Both the ordinate and abscissa are scaled by the local thickness of the outer wake shear layer, $\Delta \equiv z_e - z_m$, where z_e and z_m are the locations of the outer edge of the wake shear layer and the location of maximum wake defect, respectively. As is the case for free shear flows, the mixing length is found to vary remarkably little across the wake shear layer, and for most locations a constant value of $\ell_m/\Delta \approx 0.19$ represents a reasonable fit to the data. The most notable exception occurs for $x/c = 0.7$, which is the location of onset of full confluence. This gives rise to highly elevated values of ℓ_m near the center of the slat wake, that is, as $z \to z_m$.

IV. Conclusion

The combined flow visualization and integrated pressure measurements presented show that optimum lift behavior is associated with slat positions for which full confluence is delayed to the most aft chordwise locations on the main element. Early confluence gives rise to enhanced mixing between the viscous wall layer and slat wake that produces an increased momentum defect near the wall and an associated increase in displacement and momentum thickness over the main element. This has the effect of reducing the suction on the main element, and, consequently, lift is reduced. Thus, even in the absence of main element separation, lift is reduced as a consequence of confluence due to the associated outward streamline displacement effect.

Despite obvious differences in the confluent boundary-layer profiles from those of conventional turbulent boundary layers, it was found that, between the wall and mixing interface on the lower side of the slat wake, the mean velocity is well represented by a modified form of Cole's composite relation. The wake parameter $\Pi_*(x, \delta_w)$ is to be evaluated at the location above the wall corresponding to $\overline{u'w'} = 0$ for chordwise stations corresponding to weak confluence. For the region of full confluence, optimum values of δ_w can be obtained by extrapolation of an exponential fit to upstream values. That Eq. (1) fits the measured mean velocity profiles below the slat wake indicates that the inner region of the confluent boundary layer behaves very much like a classic turbulent boundary layer in pressure gradient but that instead of adjusting to the local inviscid freestream it adjusts to the velocity imposed on the lower side of the slat wake. This is not surprising because the near-wall dynamics occur on a timescale of order $t \propto \nu/u_\tau^2$ whereas the characteristic eddy rollover time associated with the shear layer extending from the wall to the wake is on the order of $T \propto U_w/\delta_w$. Based on the experiments, the ratio of these timescales is found to be $T/t = \delta_w^+/U_w^+ \approx 5$. As a consequence, the lower slat shear layer presents a quasi-static local condition for the more rapid dynamics of the near-wall region of the confluent boundary layer to adjust to.

Despite the adverse pressure gradient environment, the outer wake shear layer is found to exhibit mean flow similarity when scaled by the local vorticity thickness and maximum wake defect. In contrast, the local mean velocity at z locations associated with the interface between the viscous wall layer and lower slat wake shear layer exhibits a strong variation in the streamwise direction that prohibits any type of similarity scaling. This is the same region that was found to exhibit countergradient momentum transport. Note that negative values of $-\overline{u'w'}\,\partial\bar{U}/\partial z$ were found to be associated with locations for which the wake is not fully mixed with the wall layer and the lower wake shear layer remains distinct. That countergradient momentum transport occurs only in the initial stages of mixing suggests that the interaction between large-scale vorticity shed by the slat wake and the large-scale structure associated with the outer portion of the viscous wall layer plays an important role. This is qualitatively consistent with the mechanism for countergradient transport postulated by Hinze.[17]

Finally, the experimental results presented represent only a small fraction of a large archival database that has been obtained on the development of a confluent boundary layer under geometric and pressure gradient conditions quite similar to those occurring in actual high-lift systems. This data set provides a unique opportunity to perform benchmark numerical simulations of confluent boundary-layer development and to investigate the suitability of various turbulence models. Although the Reynolds number of the experiment is comparatively low, we feel that this represents a very complete, nonintrusively obtained data set of high integrity that includes the influence of both strong and comparatively weak confluence. As such, it should provide a suitable challenge to current predictive schemes despite the modest Reynolds number. The authors will be happy to provide access to the full database to those readers interested in performing their own CFD simulations.

Acknowledgments

This research effort was supported by NASA Ames Research Center, Moffett Field, California, under Grant NASA-NAG2-905. The authors wish to express their appreciation to Larry Erickson and Dale Satran of NASA Ames Research Center for their assistance and suggestions during the course of the study. The authors also wish to thank Peter Chu, who was involved with the flow visualization work, as well as surface pressure and initial laser Doppler velocimetry measurements.

References

[1] Smith, A. M. O., "High-Lift Aerodynamics," *Journal of Aircraft*, Vol. 12, No. 6, 1975, pp. 501–530.

[2] Klausmeyer, S. M., and Lin, J. C., "Comparative Results from a CFD Challenge Over a 2D Three-Element High-Lift Airfoil," NASA TM 112858, 1997.

[3] Nakayama, A., Kreplin, H. P., and Morgan, H. L., "Experimental Investigation of Flowfield About a Multielement Airfoil," *AIAA Journal*, Vol. 28, No. 1, 1990, pp. 14–21.

[4] Mack, M. D., and McMasters, J. H., "High Reynolds Number Testing in Support of Transport Airplane Development," AIAA Paper 92-3982, 1992.

[5]Chin, V. D., Peters, D. W., Spaid, F. W., and McGhee, R. J., "Flowfield Measurements About a Multi-Element Airfoil at High Reynolds Numbers," AIAA Paper 93-3137, 1993.

[6]Bario, F., Charnay, G., and Papailiou, K. D., "An Experiment Concerning the Confluence of a Wake and a Boundary Layer," *Journal of Fluids Engineering*, Vol. 104, No. 1, 1982, pp. 18–24.

[7]Zhou, M. D., and Squire, L. C., "The Interaction of a Wake with a Boundary Layer," *Structure of Complex Turbulent Shear Flow*, edited by R. Dumas and L. Fulachier, Springer–Verlag, New York, 1983, pp. 376–387.

[8]Zhou, M. D., and Squire, L. C., "The Interaction of a Wake with a Turbulent Boundary Layer," *Aeronautical Journal*, Vol. 89, No. 882, 1985, pp. 72–81.

[9]Agoropoulos, D., and Squire, L. C., "Interactions Between Turbulent Wakes and Boundary Layers," *AIAA Journal*, Vol. 26, No. 10, 1988, pp. 1194–1200.

[10]Moghadam, A., and Squire, L. C., "The Mixing of Three-Dimensional Turbulent Wakes and Boundary Layers," *Aeronautical Journal*, Vol. 93, No. 925, 1989, pp. 153–161.

[11]Tulapurkara, E. G., Ramjee, V., and Rajasekar, R., "Interaction Between Boundary Layer and Wakes of Different Bodies," *AIAA Journal*, Vol. 28, No. 6, 1990, pp. 1032–1037.

[12]Johnston, L. J., and Horton, H. P., "An Experimental Study of Turbulent Wake/Boundary Layer Mixing Flows," AIAA/International Council of the Aeronautical Sciences, TR 86-2.3.4, Reston, VA, Sept. 1986.

[13]Braden, J. A., Whipkey, R. R., Jones, G. S., and Lilley, D. E., "Experimental Study of the Separating Confluent Boundary Layer," NASA CR 3655, 1983.

[14]Brune, G. W., and Sikavi, D. A., "Experimental Investigation of the Confluent Boundary Layer of a Multielement Low Speed Airfoil," AIAA Paper 83-0566, 1983.

[15]Rumsey, C. L., Gatski, T. B., Ying, S. X., and Bertelrud, A., "Prediction of High-Lift Flows Using Turbulent Closure Models," AIAA Paper 97-2260, 1997.

[16]Townsend, A. A., *The Structure of Turbulent Shear Flow*, Cambridge Univ. Press, New York, 1976, Chap. 6.

[17]Hinze, J. O., "Turbulent Flow Regions with Shear Stress and Mean Velocity Gradient of Opposite Sign," *Applied Scientific Research Journal*, Vol. 22, No. 3/4, 1970, pp. 163–175.

[18]Wilcox, D. W., *Turbulence Modeling for CFD*, 2nd ed., DCW Industries, LaCanada, CA, 1998, Chap. 3.

J. P. Gore
Associate Editor